



A micromechanics study on strain-localization-induced fracture initiation in bending using crystal plasticity models

MING DAO†

Department of Materials Science and Engineering, Massachusetts Institute of Technology, Cambridge, Massachusetts, 02139, USA

and MING LI€

Material Mechanics, Thermo-mechanical Processing and Alloy Design, Alcoa Technical Center, Alcoa Center, Pennsylvania 15069, USA

[Received 15 May 2000 and accepted in revised form 25 October 2000]

ABSTRACT

A crystal-plasticity-based computational micromechanics model is presented to study the localization and fracture initiation modes in bending of sheet materials. The model accounts for the orientation-dependent non-uniform deformation within each grain. Parameters evaluated include strain hardening, second-phase particle position and distribution, and crystallographic texture. Surface roughening and localized deformation are found to result naturally from orientation and slip geometry differences across neighbouring grains. Shear bands initiate on or near the outer surface and from the low points of surface roughness. The maximum plastic strain may occur below the free surface, which is different from the predictions based on continuum elastic–plastic theories. Computational results also suggest that constituent particles, especially near the free surface, can significantly increase the localization intensity and the surface roughening. Crystallographic textures that contain high volume fractions of rolling texture components can increase the surface roughening significantly compared with a random texture. Bifurcation analysis results in further understanding of the different localization modes between the tension and the compression sides of the bending specimen. These findings from the theoretical–computational study agree well with experimental observations. They give insights into improving the bendability of aluminium sheet alloys.

§1. INTRODUCTION

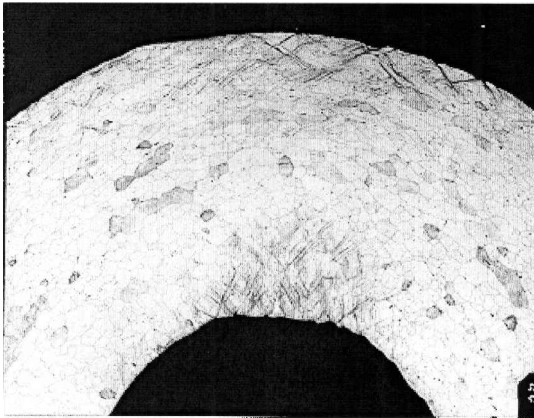
Bending is one of the most widely used operations in sheet metal forming. In the automotive industry, for example, ‘hemming’ basically is a 180°, two-step bending process to connect outer and inner automotive body panels. Bending operations of sheet materials are also used in aerospace, rigid packaging, computer, electronics and many other industries. Owing to the lower ductility and fracture resistance of aluminium alloys compared with steels, bendability and hemmability significantly restrict the application of aluminium alloy sheet in automotive body panels. Most of

† Email: mingdao@mit.edu

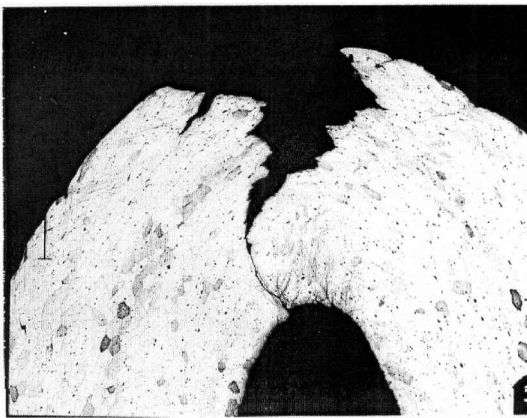
€ Email: ming.li@alcoa.com

the commonly used autobody sheet alloys for outer panels are capable of being relieved flat-hemmed (figure 1(a)) but they typically are not flat-hemmmable (figure 1(b)).

With a combined experimental, computational and theoretical approach, this paper investigates the fracture initiation micromechanisms of aluminium autobody sheet alloys. The understanding should help in the design of better aluminium sheet alloys and associated fabrication processes for autobody as well as aerospace and rigid container sheet applications. Also, the micromechanisms provide insight into developing failure criteria which are critical in simulations and predictive designs of bending and hemming processes. Experimental investigations revealed that intense strain-localization-induced fracture initiation is the major failure initiation mode in bending and hemming of aluminium sheet materials (figure 2). The focus of the



(a)



(b)

Figure 1. (a) Shear bands observed on both the tensile and the compressive sides in a relieved flat-hemmed sample; (b) fracture results in a flat-hemmed sample of an aluminium autobody sheet alloy.

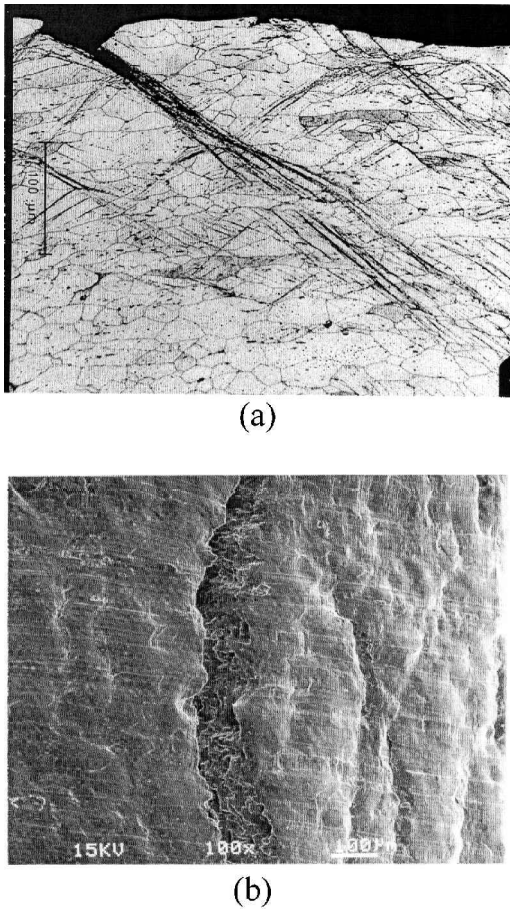


Figure 2. (a) Side view (optical micrograph) of a ductile fracture initiated by an intense shear band; (b) top view (scanning electron micrograph) of the fractured sample surface. Surface roughening is clearly shown in (b).

computational–theoretical analysis is, therefore, on the initiation and development of intense shear banding.

Another closely relevant aspect is surface roughening during forming (or deformation). Experimental (Valkonen 1987) and numerical (Beaudoin *et al.* 1998, Becker 1998) studies of sheet during stretching showed that surface roughness evolves linearly with strain and has a linear dependence on the grain size. It is most noteworthy that small-scale strain localization at the surface was found to play a significant role in surface roughening (Becker 1992, 1998) and, consequently, factors which influence strain localization also affect surface roughening. Beaudoin *et al.* (1998) found that grains with similar orientations (clusters) may act collectively to form localized regions of thinning (a form of surface roughening). The current study focuses on the intense shear band initiation and evolution during bending and hemming (instead of simple stretching). Compared with uniaxial stretching or tension, a unique feature of bending and hemming is that there is a built-in stress–strain gradient across the thickness of the sheet material. Certain technical challenges arise as a result of this stress–strain gradient. For example, the commonly employed

forming limit diagram in sheet forming is not applicable to predict failure in bending and hemming. Fracture criteria which work well under uniform stress–strain conditions predict much lower failure strains (e.g. as much as 300% error) than are observed experimentally (Li and Lege 1997).

Based on the classical framework of localization established through the work of Hadamard (1903), Hill (1962) and Rice (1977), extensive studies on the subject of localized deformation in crystalline solids have been performed (for example Asaro and Rice (1977), Harren *et al.* (1988), Bassani (1994) and Dao and Asaro (1996a, b)). It has been realized that localization of plastic flow in ductile crystals is a natural inevitable outcome of finite deformation processes. However, most of these studies assume initial uniform macroscopic stresses and strains.

On the other hand, developments of shear bands and ductile failure modes in pure bending (with a built-in stress–strain gradient) were studied using continuum elastic–plastic theories (for example Triantafyllidis and Needleman (1982) and Tvergaard (1987)). Macroscopic initial imperfections have to be introduced to trigger the shear bands, and the peak straining within the shear bands was found always to occur at the free surface.

Strain hardening, texture, second-phase particle position and distribution are considered to be the most important factors affecting the fracture initiation during the bending of aluminium sheet materials. Through normal experimental methods, these factors are not easily distinguishable. However, ‘virtual experiments’ can be performed with computational modelling and the effects of individual parameters as well as the composite effects of these parameters can be systematically studied and quantitatively evaluated. The results can provide useful insights for alloy design to mitigate fracture initiation during bending processes.

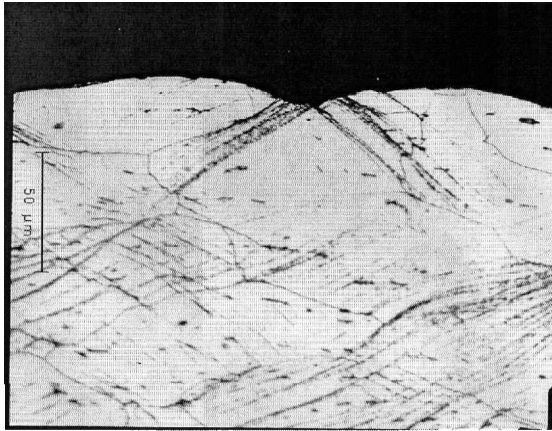
In the present work, a crystal-plasticity-based computational micromechanics model is applied to study the localization and fracture initiation modes in bending and hemming of sheet materials. The approach integrates the experimental, computational and theoretical methods.

§2. SUMMARY OF THE EXPERIMENTAL OBSERVATIONS

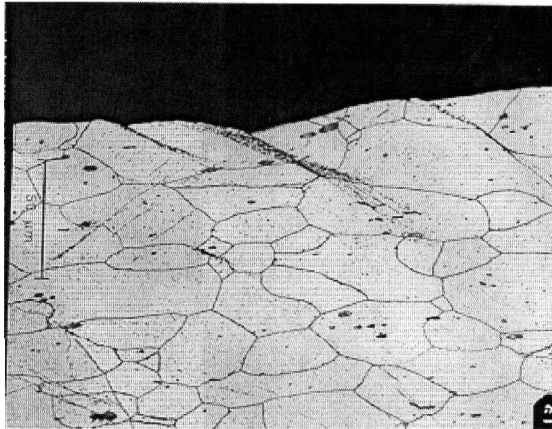
A systematic experimental investigation was conducted to understand the micro-mechanisms of fracture initiation in the bending and hemming of aluminium auto-body sheet alloys (Li 2000). A summary of the most important observations regarding the initiation and development of intense shear bands is described herein.

In figure 1 (*a*), the localized deformations are found on both the tensile and the compressive sides of the sample, and shear band angles (with respect to the free surfaces) are found to be around 40° on the tensile side and around 50° on the compressive side. Figure 1 (*b*) shows the typical fracture in the flat hemming operation. It has been found that the fracture mode is mostly transgranular (Li 2000).

The optical and scanning electron microscopy observations (figure 2) reveal that the crack appears to initiate from the surface roughness owing to plastic deformation. The dominant mechanism of failure initiation is the development of intense shear bands. These shear bands propagate through grains. Final fracture occurs when the shear bands propagate and interact with second-phase particles. This is the reason why the fracture mode is predominantly transgranular. The initiation sites for development of shear bands include surface low cusp points due to surface roughening, second phase particles, and grain boundary precipitates. As shown in figure 3, shear bands can initiate from the lower points of surface roughening.



(a)

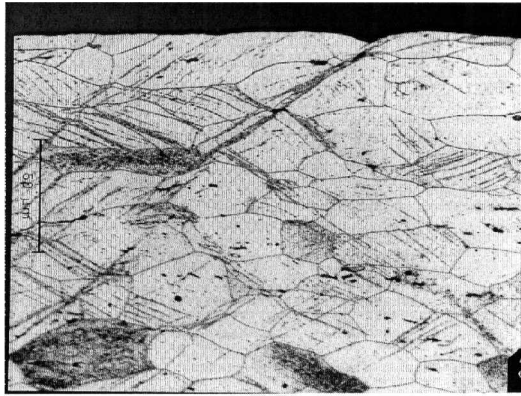


(b)

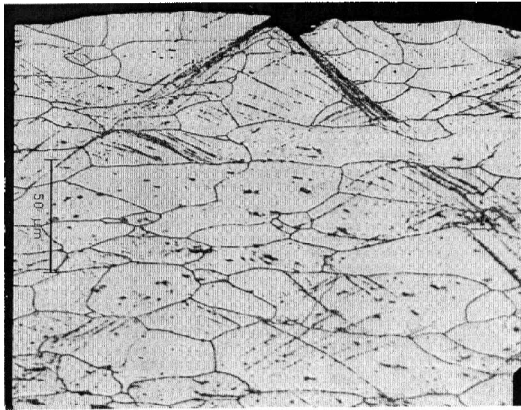
Figure 3. Localization modes near the free surface: (a) symmetrically oriented shear bands initiate from a lower cusp point due to surface roughening; (b) several nearly parallel shear bands initiate from the lower points, where these bands are also closely associated with the nearby grain corners.

However, not all lower points of the surface will initiate shear bands. Shear bands can also initiate from second-phase particles, as exhibited in figure 4(a). These particles can be well under the free surface where the material experiences the most macroscopic deformation. Another source for shear band initiation is grain-boundary precipitates (Li 2000). When the grain boundary happens to be in the direction of maximum shear and the grain boundary precipitates are in the form of an elongated shape (i.e. a plate shape), shear bands will develop and the grain boundary can separate to form microcracks.

A very interesting observation is found in figure 4(b), where a shear band jumps over two grains before continuing further. This is probably caused by the different *orientation dependent* localization modes between neighbouring grains.



(a)



(b)

Figure 4. Localization modes below the free surface: (a) shear band pairs form X-shaped patterns, and second-phase particles underneath the free surface can initiate shear bands; (b) a shear band jumps over two grains before continuing further.

§3. MODELLING APPROACH

3.1. Single-crystal constitutive model

The constitutive theory used in this analysis is a rate-dependent crystal plasticity model. The theory is developed from earlier versions by Asaro and Rice (1977), Peirce *et al.* (1983), and most recently Dao and Asaro (1996a, b). The deformation of a single crystal from the reference configuration to the current configuration can be decomposed into plastic shearing, and elastic stretching and lattice rotation. The deformation gradient \mathbf{F} is thus decomposed as

$$\mathbf{F} = \mathbf{F}^* \cdot \mathbf{F}^P, \quad (1)$$

where \mathbf{F}^P is the plastic deformation gradient which represents the shear flow of crystal through the undeformed lattice along various slip systems and \mathbf{F}^* is the elastic deformation gradient representing the elastic stretching and rigid-body rotation of the crystal.

The velocity gradient of the single crystal can be defined as

$$\mathbf{L} = \dot{\mathbf{F}} \cdot \mathbf{F}^{-1}. \quad (2)$$

The velocity gradients of plastic shear flow can be written as

$$\dot{\mathbf{F}}^P \cdot \mathbf{F}^{P-1} = \sum_{\alpha} \dot{\gamma}_{\alpha} \mathbf{s}_{\alpha} \cdot \mathbf{m}_{\alpha}, \quad (3)$$

where $\dot{\gamma}_{\alpha}$ is the shear rate on the α th slip system; the α th slip system is defined by its slip direction \mathbf{s}_{α} and its slip plane normal \mathbf{m}_{α} .

The shear rate $\dot{\gamma}_{\alpha}$ on the slip system α in equation (3) is taken to be in the following form:

$$\dot{\gamma}_{\alpha} = \dot{\gamma}_0 \operatorname{sgn}(\tau_{\alpha}) \left(\left| \frac{\tau_{\alpha}}{g_{\alpha}} \right| \right)^{1/m}, \quad (4)$$

where τ_{α} is the current value of the resolved shear stress, $g_{\alpha} > 0$ is the current value of the slip resistance, m is the material rate sensitivity exponent (which will be taken the same for all slip systems) and $\dot{\gamma}_0$ is a reference shear rate. The resolved shear stress τ_{α} of the slip system α is given as

$$\tau_{\alpha} = \mathbf{m}_{\alpha}^* \cdot \boldsymbol{\tau} \cdot \mathbf{s}_{\alpha}^*, \quad (5)$$

where

$$\mathbf{s}_{\alpha}^* = \mathbf{F}^* \cdot \mathbf{s}_{\alpha}, \quad \mathbf{m}_{\alpha}^* = \mathbf{m}_{\alpha} \cdot \mathbf{F}^*, \quad \boldsymbol{\tau} = J\boldsymbol{\sigma}, \quad (6)$$

in which $J = \det \mathbf{F}$ is the Jacobian, $\boldsymbol{\tau}$ is the Kirchhoff stress tensor, $\boldsymbol{\sigma}$ is the Cauchy stress tensor, \mathbf{s}_{α}^* is along the α th slip direction in the current configuration and \mathbf{m}_{α}^* is normal to the α th slip plane.

The slip resistance g_{α} is obtained by the path-dependent integration of the evolution equation

$$\dot{g}_{\alpha} = \sum_{\beta} h_{\alpha\beta}(\gamma_a) |\dot{\gamma}_{\beta}|, \quad \gamma_a = \int_0^t \sum_{\alpha} |\dot{\gamma}_{\alpha}| dt, \quad (7)$$

where $h_{\alpha\beta}$ is a matrix of hardening moduli and γ_a is the accumulated sum of slips. The initial conditions for this evolution are given by $g_{\alpha} = g_{\alpha}(\gamma_a = 0) = g_{\alpha}^0$. The specific form of the hardening matrix is taken as

$$h_{\alpha\beta} = qh + (1 - q)h\delta_{\alpha\beta}, \quad (8)$$

where q sets the level of latent hardening to the self-hardening of the slip system and h is the self-hardening rate. Other forms of the latent hardening relations may be used, in particular those recently developed by Wu *et al.* (1991) and Cuitino and Ortiz (1993).

The constitutive description of the single crystal is completed with a specification of its elasticity. Here, we consider the elastic anisotropy of the single crystal and assume the following form:

$$\dot{\mathbf{S}}^* = \mathbf{K} : \dot{\mathbf{E}}^*, \quad (9)$$

where $\mathbf{S}^* = \mathbf{F}^{*-1} \cdot \boldsymbol{\tau} \cdot \mathbf{F}^{*-T}$ is the lattice-based second Piola–Kirchhoff stress, $\mathbf{E}^* = (\mathbf{F}^{*T} \cdot \mathbf{F}^* - \mathbf{I})/2$ is the Green strain of the lattice and \mathbf{I} is the second-order identity tensor. The final constitutive theory is then expressed in terms of the second

Piola–Kirchhoff stress $\mathbf{S} = \mathbf{F}^{-1} \cdot \boldsymbol{\tau} \cdot \mathbf{F}^{-T}$, and the Green strain $\mathbf{E} = (\mathbf{F}^T \cdot \mathbf{F} - \mathbf{I})/2$. Straightforward manipulation of the above equations gives the rate form of the governing constitutive equation

$$\dot{\mathbf{S}} = \mathbf{L} : \dot{\mathbf{E}} - \sum_{\alpha} \dot{\gamma}_{\alpha} \mathbf{X}_{\alpha}, \tag{10}$$

where

$$\begin{aligned} L_{ijrn} &= \sum_k \sum_l \sum_p \sum_q F_{ik}^{P-1} F_{jl}^{P-1} K_{klpq} F_{rp}^{P-1} F_{nq}^{P-1} \\ \mathbf{X}_{\alpha} &= \mathbf{F}^{P-1} \cdot (\mathbf{K} : \mathbf{A}_{\alpha} + 2\mathbf{H}_{\alpha}) \cdot \mathbf{F}^{P-T}, \\ \mathbf{A}_{\alpha} &= \text{sym} [\mathbf{F}^{*T} \cdot \mathbf{F}^* \cdot (\mathbf{s}_{\alpha} \cdot \mathbf{m}_{\alpha})] \\ \mathbf{H}_{\alpha} &= \text{sym} [(\mathbf{s}_{\alpha} \cdot \mathbf{m}_{\alpha}) \cdot \mathbf{S}^*], \end{aligned} \tag{11}$$

where $\text{sym}[\cdot]$ means the symmetric part of $[\cdot]$. The details of the derivation of equations (10) and (11) may be found elsewhere (for example McHugh *et al.* (1993) and Dao and Asaro (1996b)) and are omitted here. The crystal plasticity model is then implemented into the user-defined material subroutine UMAT available in the commercial finite element package ABAQUS (1998).

3.2. Computational micromechanics model set-up

A micromechanics model is constructed to study the localized deformation modes developed in a bending specimen. Figure 5 (a) shows the schematic drawing

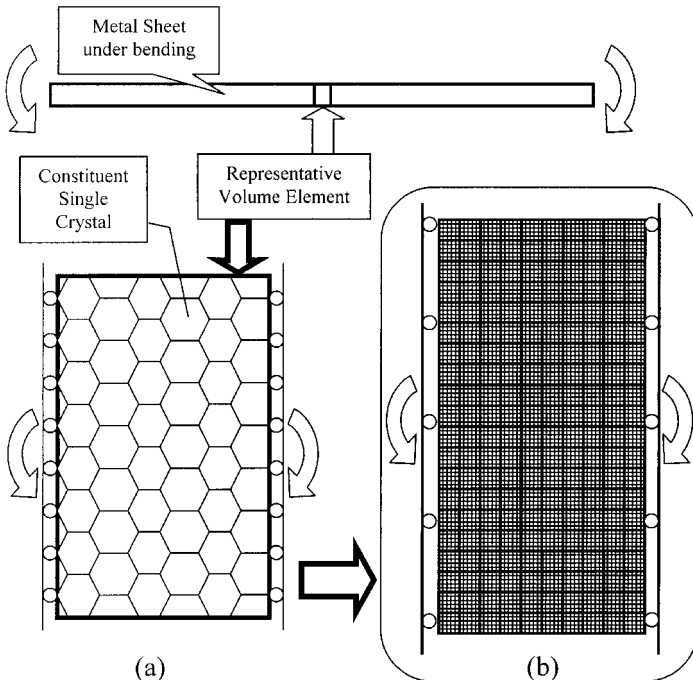


Figure 5. (a) Schematic drawing of the micromechanics model for a polycrystal specimen under pure bending; (b) original mesh with 200 grains modelled with 5000 rectangular elements.

of the representative volume element (RVE). This RVE is subjected to a pure bending boundary condition. Figure 5(b) shows the original finite-element mesh used in the study. 200 grains were modelled within a $500\ \mu\text{m} \times 1000\ \mu\text{m}$ (width \times thickness) rectangular region, which represents a grain size of the order of $50\ \mu\text{m}$. Several calculation runs using larger aspect ratios (width-to-thickness ratio factors of four and two larger) were also made; the deformation patterns were found to be similar to the original model shown in figure 5(b). It is noted that the possible troublesome spots are essentially the four grains at the corners of the mesh because of the bending conditions. For these four grains, an implicit assumption is that each grain has a neighbouring grain with a mirrored orientation. Within a multicrystal aggregate, this should be a close approximation to certain common situations in reality, although it may or may not be the strongest stress concentration situation. The localization pattern thus may or may not be directly associated with the corners (boundaries), as confirmed by computations.

Another implicit assumption of the model is that no grain-boundary sliding occurs during the deformation. In general, grain boundary sliding is a mechanism of plastic deformation under low stresses and at elevated temperatures (for example Raj and Ashby (1975) and Ashby and Verrall (1977)). Under high stresses and at room temperature, as in the forming processes discussed here, grain boundary sliding normally is not a concern. Certainly, for some heat-treatable aluminium alloys such as Al–Zn–Mg when a measurable grain-boundary precipitate free zone (PFZ) exists, neighbouring grains can slide relative to each other even at room temperature, as observed by Graf and Hornbogen (1977), because the PFZ is a layer of material much softer than the grain interior. A model has recently been proposed to study the effects of the PFZ width, the size of the grain boundary precipitate and the grain size on intergranular fracture (Li and Butler 1999). However, for most aluminium alloys such as those used in the experiments cited in this paper (Li 2000), the PFZ is so thin that it probably does not exist.

All of the 5000 elements are four-node isoparametric quadrilaterals with selected reduced integration on the pressure. The mesh is continuous across grain boundaries where grain boundary sliding is not allowed. This is a continuum theory where the initial configuration is taken as stress free and without any lattice perturbations. In fact, each grain boundary is a line across which the initial crystallographic orientations (i.e. Euler angles) have a jump. The mesh is subjected to a pure bending boundary condition, as illustrated in figure 5(b). The rectangular grain shape is used for the convenience of the mesh generation. H. Dai and D. M. Parks (1998, private communication) discussed in detail the effects of different grain morphologies within a crystal plasticity based multicrystal aggregate, and the rectangular grain shape is considered a reasonable assumption for calculating the macroscopic behaviour and the general non-uniform deformation patterns.

While three-dimensional slip geometry is modelled using the 12 $\{111\}\langle 110 \rangle$ fcc slip systems, a two-dimensional plane-strain idealization is used in the numerical simulation. Potential out-of-plane shears are constrained and spatial variations behind or in front of the model plane are neglected. These idealizations can affect the deformation field and texture evolution (for example Becker and Panchanadeeswaran (1995)). From a continuum mechanics point of view, bending of a thin sheet can be reasonably modelled as plane strain due to the apparent stress and strain states. The finite element modelling of localized deformation in a polycrystal aggregate under the plane-strain condition using 12 fcc slip systems has been

performed by Kalidindi *et al.* (1992). In that study, the accompanying Taylor model (full three-dimensional) study and experiments confirmed that both texture developments and stress–strain behaviour agree well with the plane strain finite element model. The same treatments in terms of stress-state and boundary conditions are taken here in this idealized model. It is therefore expected that the model assumptions are reasonable, at least as a first-order approximation for this particular case. However, care has to be taken when making plane-strain idealizations.

Two types of initial crystallographic texture are considered in this study. The first is a random texture (figure 6 (a)), and the second is a typical rolling–plane-strain compression texture (figure 6 (b)). The rolling texture is produced by a 50% plane-strain compression using a Taylor-like polycrystal model presented by Dao *et al.* (1996). In most of the computations, the random texture is assumed. The microstructure with a typical rolling texture is also explored to demonstrate the possible effects of texture.

The baseline material properties are measured from a aluminium alloy 6111-T4 sheet. The material is recrystallized with an average grain size of the order of 40–50 μm . Young's modulus E is 68.95 GPa and Poisson's ratio ν is 0.33. The macroscopic true stress–effective strain data experimentally determined with an equal biaxial hydraulic bulge test fit the following Voce equation well

$$\sigma \text{ (MPa)} = 421.698 - 233.947 \exp(-8.638\varepsilon). \quad (12)$$

The macroscopic stress–strain behaviour is shown in figure 7. For the computations carried out, the slip resistance g_α of all the 12 fcc slip systems at a material point is taken to be the same, that is $q = 1$ in equation (8). This is the well known Taylor hardening assumption. The evolution of the slip system hardening is assumed to follow the macroscopic hardening behaviour. Taking the average Taylor factor to be 3, the slip system hardness g_α in equation (7) can be given as

$$g_\alpha \text{ (MPa)} = 140.57 - 77.98 \exp(-2.879\gamma_a). \quad (13)$$

The (positive) slip system hardening function $h(\gamma_a)$ is therefore

$$h(\gamma_a) = h_\alpha(\gamma_a) = \frac{\partial g_\alpha}{\partial \gamma_a} = 224.5 \exp(-2.879\gamma_a). \quad (14)$$

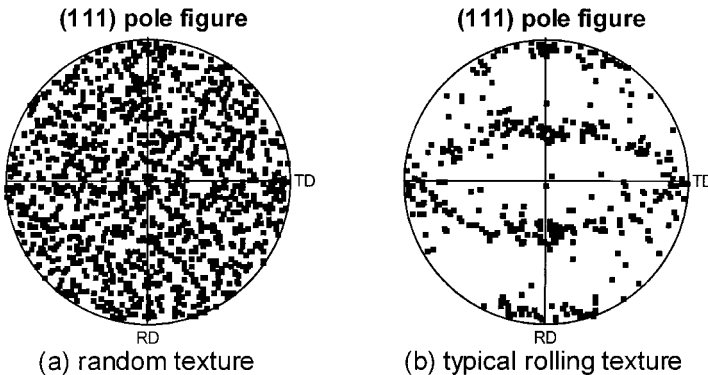


Figure 6. Crystallographic textures used in the study.

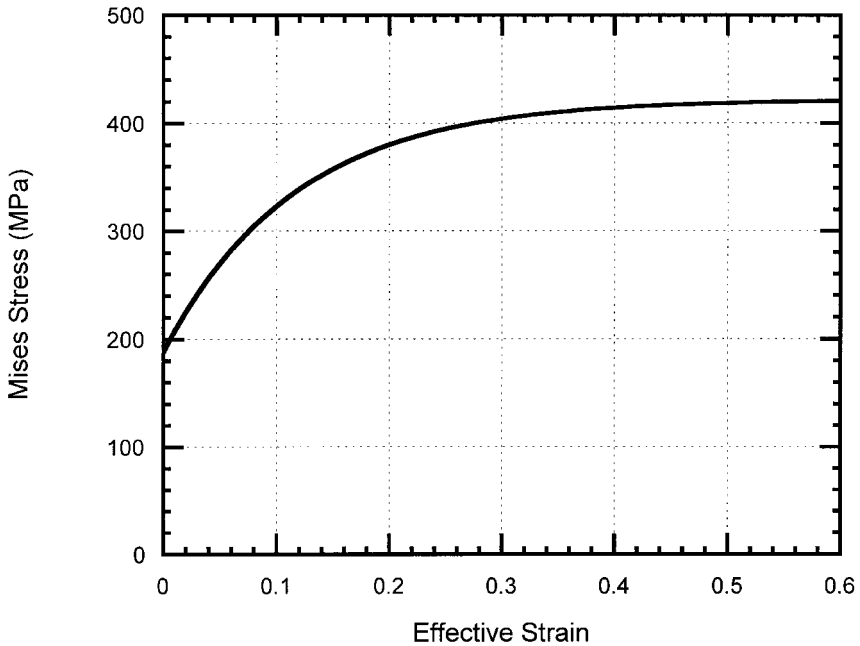


Figure 7. Macroscopic stress–strain behaviour of aluminium alloy 6111-T4 sheet.

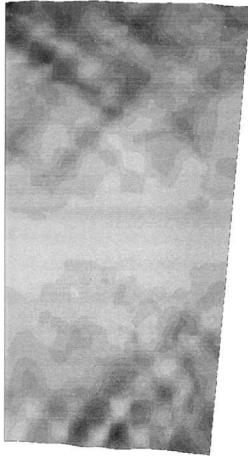
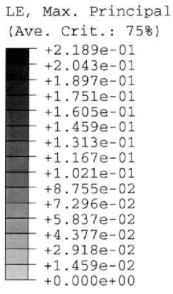
The material rate-sensitivity exponent m is assumed to be 0.01, and the reference shear rate $\dot{\gamma}_0$ is 0.03 s^{-1} . In normal forming processes, the strain rate of deformation is in the range $0.001\text{--}0.1 \text{ s}^{-1}$. In the experiments cited in this paper, the punch speed to perform the bending was 0.05 m s^{-1} , which translates into the strain rate of the order of 0.01 s^{-1} in the deformation zone. From our experience with aluminium alloys, the plastic deformation of aluminium alloys at room temperature is rather rate insensitive for a wide strain rate range from 0.001 to 10 s^{-1} . Just as a reference, the strain rate sensitivity of aluminium alloys is normally several orders lower than that of carbon steels.

§4. COMPUTATIONAL RESULTS: MICROSTRUCTURES WITHOUT CONSTITUENT PARTICLES

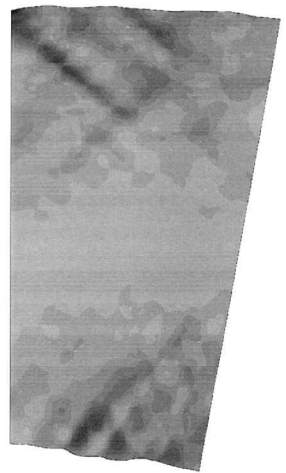
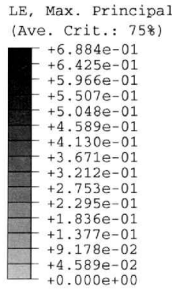
To study the localized deformation patterns, several randomly generated initial textures are studied using the baseline material properties as well as higher hardening parameters in this section. In general, two typical localization patterns result from random textures, designated case 1 and case 2. Case 1 is a parallel localization pattern (figure 8) with a corresponding randomly generated texture T1. Case 2 is an intersecting localization pattern (figure 9) with a corresponding randomly generated texture T2. The localized deformation patterns are computed without assuming any initial geometric imperfections.

4.1. Non-uniform deformation patterns

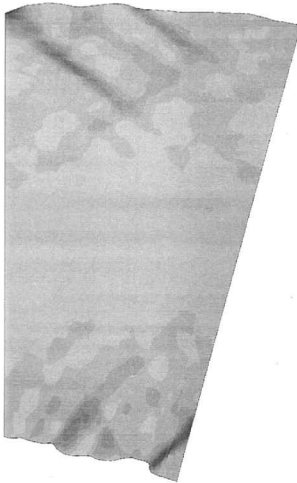
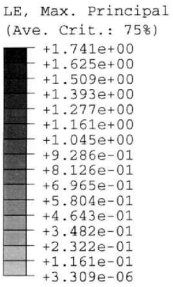
Figure 8 shows the evolution of localized deformation patterns (baseline case 1) using the randomly generated initial texture T1 shown in figure 6(a). At a bending angle of 5° (figure 8(a)), the deformation is already highly non-uniform although



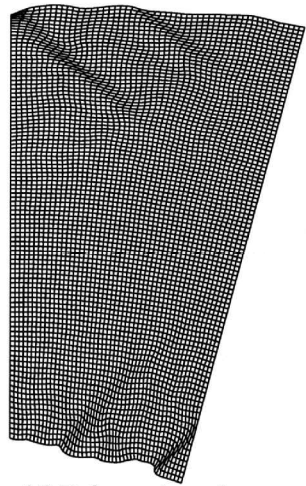
(a) Maximum principle strain
Rotation = 5 degrees



(b) Maximum principle strain
Rotation = 10 degrees



(c) Maximum principle strain
Rotation = 15 degrees



(d) Deformed mesh
Rotation = 15 degrees

Figure 8. Development of localized deformation patterns for the baseline case 1.

intense macroscopic shear bands are not yet fully developed. After bending 10° (figure 8(b)), several macroscopic shear bands are readily identified on both the tensile side and the compressive side. At a bending angle of 15° (figures 8(c) and (d)), the intense macroscopic shear bands are fully developed, and the surface roughening is clearly observed. The surface roughening and intense shear banding are the natural outcome of the polycrystalline microstructure. As can be seen from figures 8(c) and (d), intense shear bands always initiate from the lower points on the surface, but not every lower point initiates an intense shear band. The shear band angles with

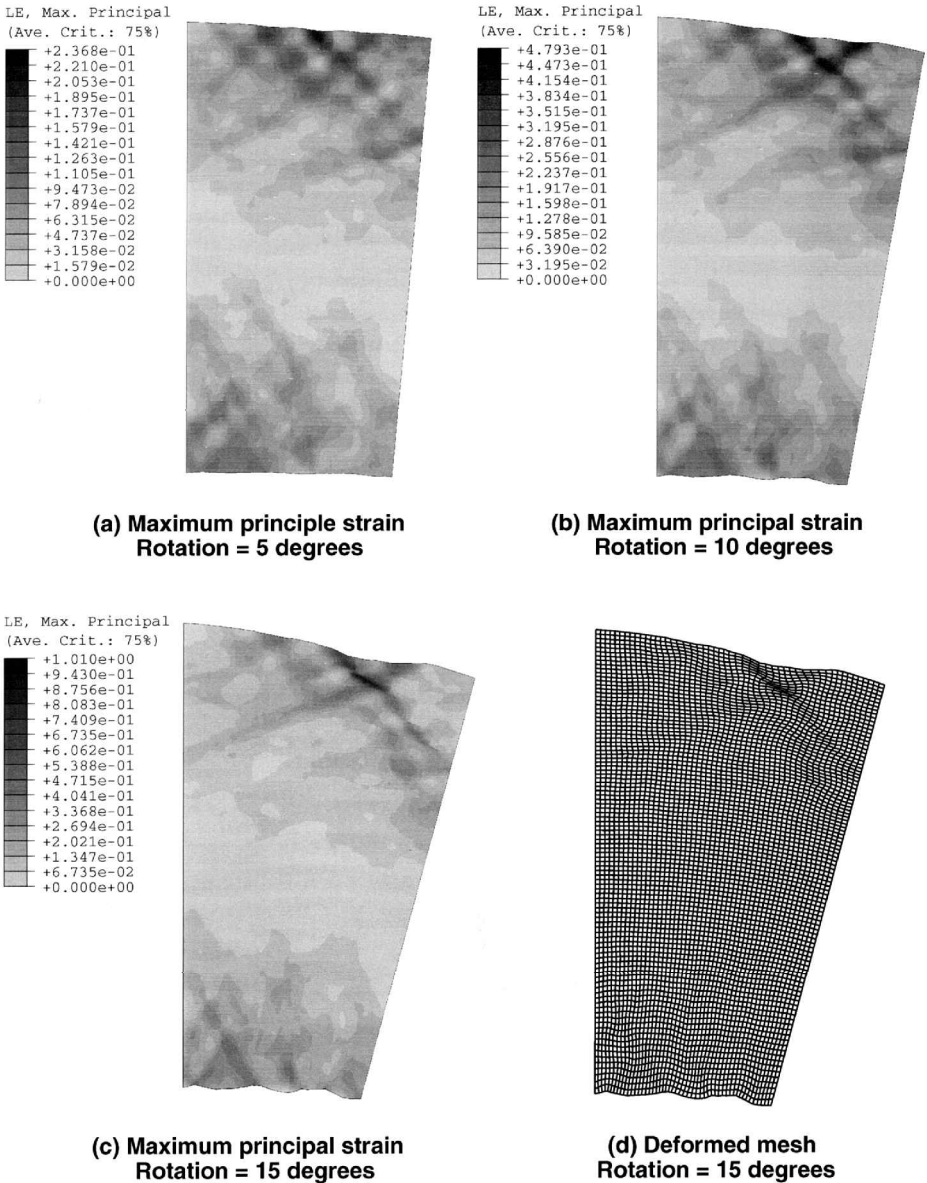


Figure 9. Development of localized deformation patterns for the baseline case 2.

respect to the free surface on the tensile side are around 40° , while the angles on the compressive side are around 50° . The shear bands initiate at similar (global) bending deformation levels from both the tensile and the compressive sides. The maximum principal strains ϵ_p^3 accumulated in these intense shear bands are of the order of 100% or higher, which is likely to initiate ductile shear failure along the shear band path.

To explore possible ‘sample variations’ in our computational ‘virtual experiments’, a number of differently randomly generated crystallographic textures are

studied. Figure 9 shows a set of typical results from another randomly generated initial texture T2 (baseline case 2). In this case, an X-shaped shear band pair forms in the middle on the top surface. The evolution of the localization process is similar to that of the baseline case 1. Again, at a bending angle of 5° (figure 9(a)), the deformation is already highly non-uniform although intense macroscopic shear bands are not yet fully developed at this early stage. After bending 10° (figure 9(b)), several macroscopic shear bands on both the tensile side and the compressive side are readily identified. Finally, at a bending angle of 15° (figures 9(c) and (d)), the intense macroscopic shear bands are fully developed, and the surface roughening is clearly observed at this stage. The surface roughening and intense shear banding are, again, the natural outcome of the polycrystalline microstructure, and intense shear bands always initiate from the lower surface points. The shear band angles with respect to the free surface on the tensile side are around 40° , while the angles on the compressive side are around 50° . The maximum principal strains e_p^3 accumulated in these intense shear bands are of the order of 60–100%, which is lower than observed in baseline case 1. It is interesting to observe that the peak maximum principal strain is located at the centre of the intersecting shear bands, which is below the free surface. Deve *et al.* (1988) reported that the intensive shear strain accumulation at the intersection of two shear bands can lead to fracture. Similar observations were made by Chang (1979) and Chang and Asaro (1981). Figure 10 shows the development of the peak e_p^3 (maximum principal strain) in the microstructure versus bending angle for the two cases studied. Baseline case 2 (with the intersecting localization pattern (figure 9)) has a lower peak strain than baseline case 1 (shown in figure 8).

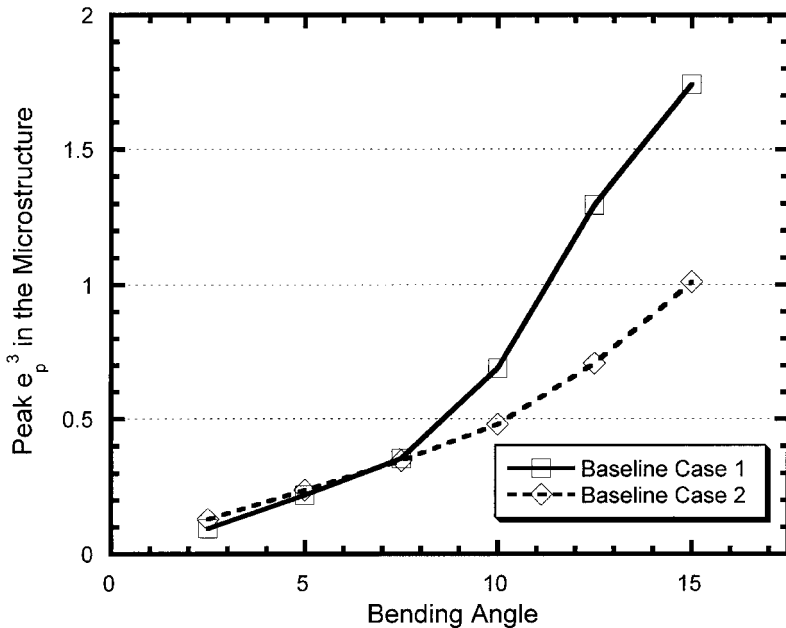


Figure 10. Evolution of the peak e_p^3 (maximum principal strain) versus the bending angle for the two baseline cases.

On examining the von Mises stress distribution across different grains as well as within each grain at a small bending angle of 0.25° , the stress distribution is clearly non-uniform and crystallographic orientation dependent (figure not shown). The contour plot of e_p^3 (maximum principal strain) at the same bending angle shows that the deformation is already quite non-uniform at this very early stage (figure not shown). This is expected from the inhomogeneities across neighbouring grains within the model microstructure.

Additional cases with different random textures were studied. The localization patterns observed in figures 8 and 9 were found to be typical, as were the developments of intense shear band formation.

4.2. Effects of the strain hardening

It is well known that strain hardening plays a critical role in the onset and development of localized deformation. To study the effects of strain hardening, with all other material and model parameters remaining unchanged, the hardening function $h(\gamma_a)$ was increased to be three times the baseline case, for example

$$h_{\text{new}}(\gamma_a) = 3h_{\text{base}}(\gamma_a). \quad (15)$$

Two cases are studied: case H1 and case H2. For case H1, except for $h = 3h_{\text{base}}$, all other model properties including the initial texture are taken to be the same as those used in baseline case 1. Similarly, for case H2, the only different parameter given is $h = 3h_{\text{base}}$ compared with baseline case 2. Figure 11 shows the changes in peak e_p^3 (maximum principal strain) for both case H1 and case H2. A reduction of 10–35% in peak strain is observed. Note that baseline case 1 has a much higher peak strain (i.e. more intense shear band) than baseline case 2. The effect of increasing the hardening

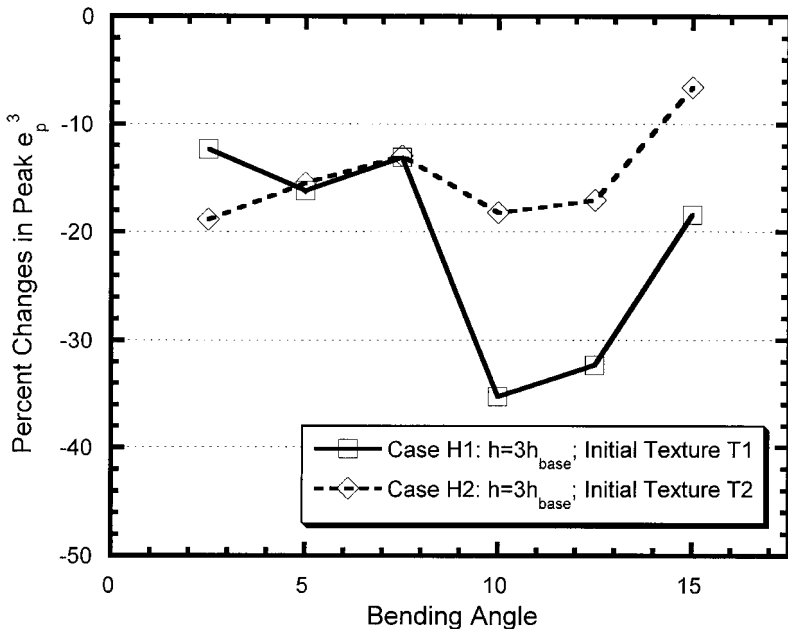


Figure 11. Effects of the hardening. The strain-hardening rate is a most important parameter that can limit the development of the localized deformation.

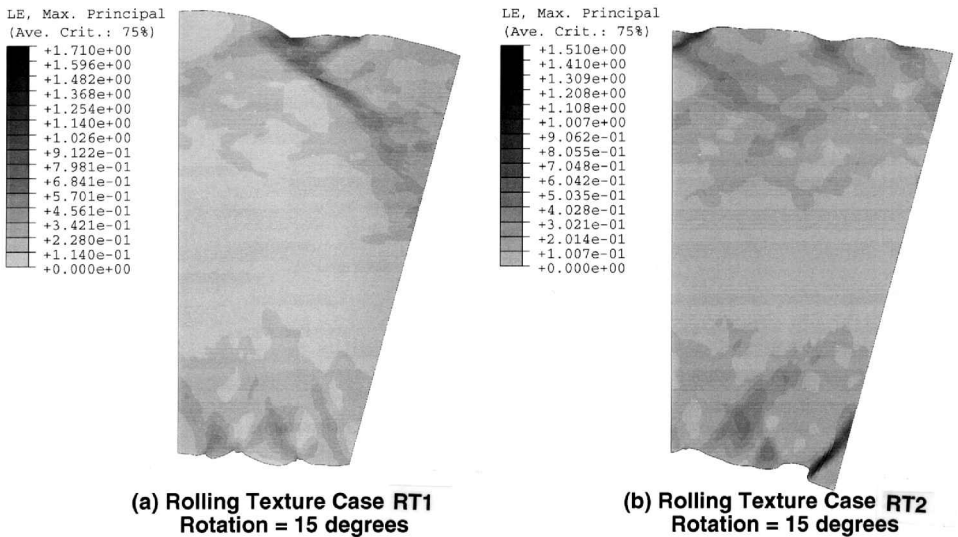


Figure 12. Effects of the rolling texture components towards localized deformation and surface roughening at a bending angle of 15° .

rate is more significant for case H1 than for case H2, especially at larger bending angles. This effect is expected, since higher strain hardening plays a strong role in reducing the intensity of localization.

4.3. *Effects of the rolling texture components*

A typical rolling texture shown in figure 6 (b) is introduced to study the effects of a rolling texture versus a random texture. Two cases, namely case RT1 and case RT2, are studied with the same overall texture but with different (random) distributions of the 200 grains in the model. Figure 12 shows the development of localized deformation and the surface roughening at a bending angle of 15° . Comparing figures 12 (a) and (b) with figures 8 (c) and 9 (c), respectively, it is evident that a typical rolling texture with medium intensity results in more severe surface roughening than a random texture.

§ 5. COMPUTATIONAL RESULTS: MICROSTRUCTURES WITH CONSTITUENT PARTICLES

5.1. *Effects of the randomly distributed particles*

This section focuses on the effects of constituent particles. Again, two typical cases were studied: case R1 and case R2. Case R1 used initial texture T1, and case R2 used initial texture T2. We note that, without any constituent particles introduced, initial texture T1 resulted a parallel localization pattern and initial texture T2 resulted an intersecting localization pattern. Baseline material properties remain the same as used in § 4. An attempt is made to understand the ‘composite effects’ of different factors, especially particle distribution and depth.

Constituent particles are modelled as hard elastic particles. Young’s modulus of the particles is assumed to be ten times that of the surrounding crystals, so that they are almost ‘rigid’ compared with the matrix material. Each particle is modelled by replacing an element in figure 5 (b) with the stiff elasticity properties. In general, the

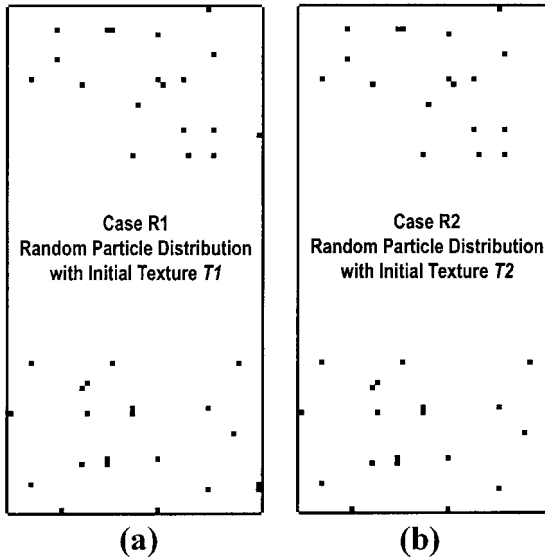


Figure 13. Microstructure models with randomly generated constituent particles. See text for details.

second-phase particles in aluminium alloys include constituents, dispersoids, and precipitates, among which the size of the constituent particles is the largest.

A typical randomly generated particle distribution geometry was used for both case R1 and case R2 as illustrated in figure 13. The particles were randomly generated according to the following rules.

- (i) Every grain has a 33% possibility of containing a particle.
- (ii) If a grain contains a particle, it would be placed randomly at one of the four corners.
- (iii) No particles are placed near the neutral axis (because very little activity is expected there).

It is noted that the number of ‘soft metal’ elements surrounding a stiff particle would not be sufficient to capture all the fine details of the localization pattern near the particle, although qualitative conclusions can be drawn carefully based on this quantitative approach.

Figure 14 shows the localized deformation results at a bending angle of 15° for the two cases. Comparing figure 14(a) with figure 8(c), the surface roughening is essentially not affected by the particles in case R1. However, comparing figure 14(b) with figure 9(c), the surface roughening is significantly affected by the particles on the free surface. Figure 15 shows the changes in peak strains due to the presence of the randomly distributed hard particles. We note that there are two competing mechanisms due to the presence of hard particles:

- (i) the *inhomogeneity* effect, where the heterogeneous microstructure tends to increase the intensity of the non-uniform and localized deformation;

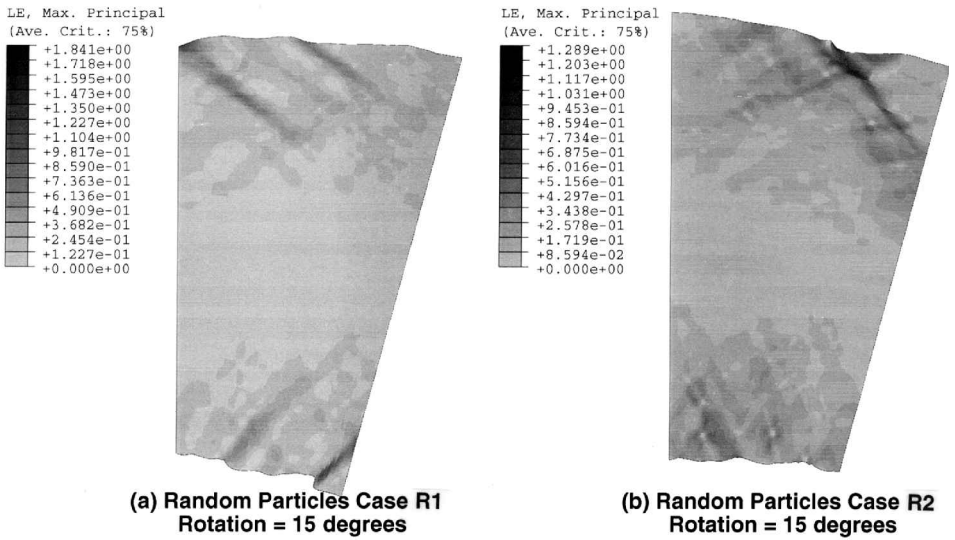


Figure 14. Localized deformation and surface roughening patterns developed in two of the model microstructures with randomly distributed particles at a bending angle of 15°.

(ii) the *strengthening* effect, where the hard particles (when there is no debonding) may reinforce the neighbouring matrix material and limit the development of intense shear bands.

The transition from the strengthening effect to the inhomogeneity effect is clearly observed in case R2 (figure 15), while in case R1 the inhomogeneity effect dominated

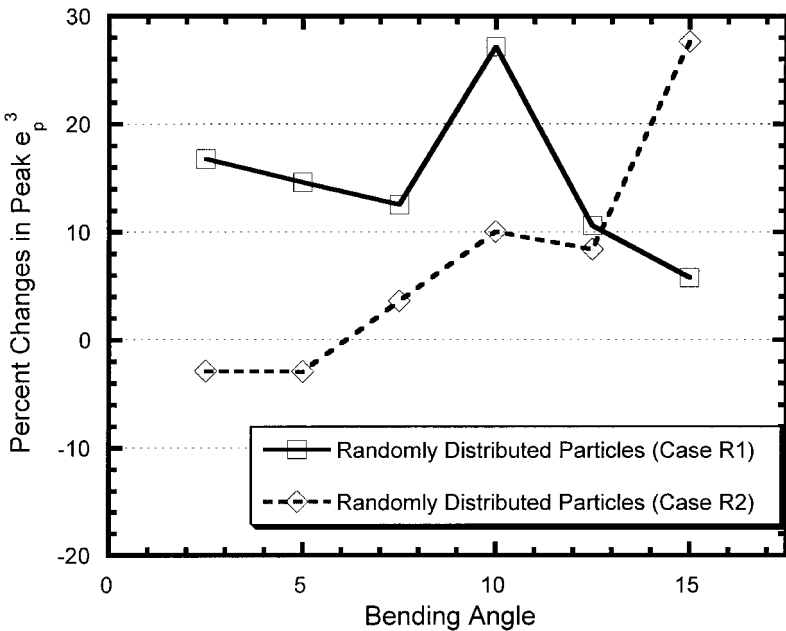


Figure 15. Effects of the randomly distributed particles towards the localization intensity.

throughout the bending deformation. Normally the inhomogeneity effect is the more dominant mechanism of the two.

5.2. Effects of the particle distribution and position

To study the effects of particle distribution and position, a number of calculations may be performed. First, a microstructure with particles randomly distributed *only* within the surface grains would be constructed, say microstructure P_1^S . Then a companion microstructure P_1^B would be constructed by shifting all the particles in P_1^S $100\ \mu\text{m}$ (twice the grain size, i.e. $2\ \text{GS}$) further below the free surface. A number of such microstructure pairs ((P_i^S, P_i^B) , $i = 1, 2, \dots, N$) can be so constructed with different random seeds. The computational results of microstructure P_i^S would be compared with that of P_i^B . This exercise again showed the competition of the two mechanisms, that is inhomogeneity versus strengthening. The inhomogeneity effect would be most likely to dominate, especially at larger strain levels. In general, the peak e_p^3 plots indicate that localization intensity would be much lower for particles embedded only a few grain sizes below the free surface than for those particles placed on or very close to the surface.

Figures 16(a) and (b) illustrate one pair of such generated microstructure pairs PS1 and PB1. Figure 16(c) shows the evolution of peak e_p^3 normalized by the com-

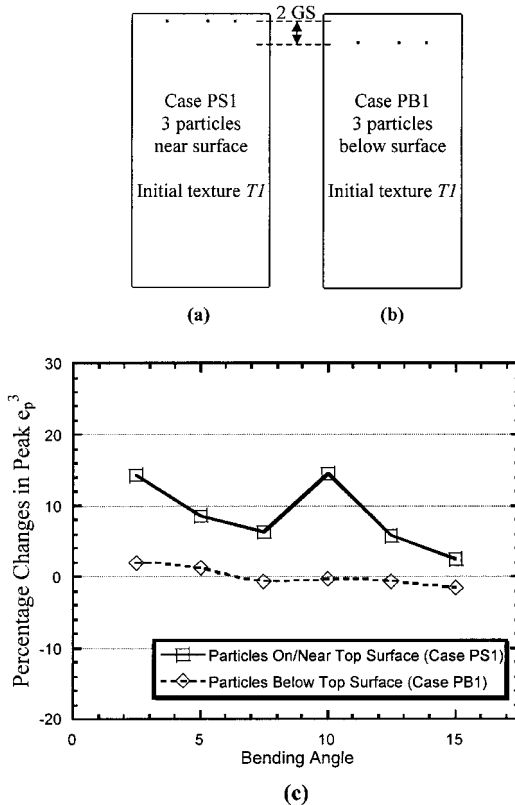


Figure 16. (a), (b) One of the generated microstructure pairs PS1 and PB1. In (b), the three particles in (a) near the bending-side free surface are shifted two grain sizes ($2\ \text{GS}$) further below. (c) The evolution of peak e_p^3 normalized by the computed values when no particles are present in the microstructure.

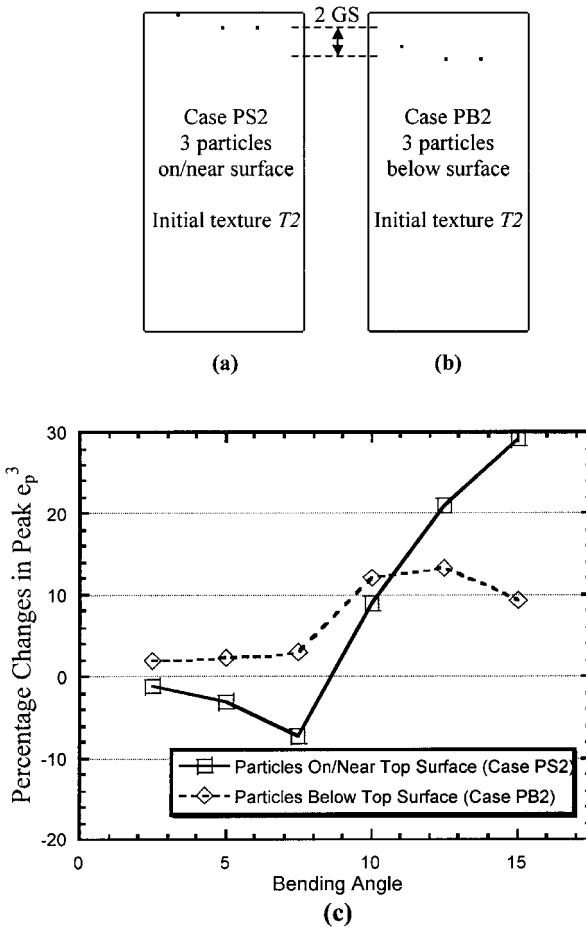


Figure 17. (a), (b) One of the generated microstructure pairs PS2 and PB2. In (b), the three particles in (a) on or near the bending-side free surface are shifted two grain sizes (2 GS) further below. (c) The evolution of peak e_p^3 normalized by the computed values when no particles are present in the microstructure.

puted values when no particles were present. It is clear that, for this case, the particles placed below the free surface have a much smaller influence on the development of localization.

Figures 17(a) and (b) illustrate another pair of such generated microstructure pairs PS2 and PB2. Figure 17(c) shows the changes in peak e_p^3 normalized by the computed values when there are no particles in the microstructure. The solid curve in figure 17(c) is the evolution function when particles are placed on or near the free surface. It is interesting to observe again the competition between the two mechanisms (inhomogeneity versus strengthening); the strengthening effect dominated early on before the inhomogeneity effect took over. The broken curve in figure 17(c) illustrates the evolution when particles are placed 100 μm below the free surface. The inhomogeneity effect dominates in this case, and again the particles placed below the free surface have a much smaller influence on the localization development.

§ 6. DISCUSSION AND CONCLUSIONS

6.1. A classical perspective on localized deformation in bending

If the constitutive law is idealized to be rate independent, Hill (1962) and Rice (1977) have given a general theory of bifurcation of a homogeneous elastic–plastic flow field into localized planar band deformation. For this to occur there is first the kinematical restriction that for localization in a thin planar band with unit normal \mathbf{n} the velocity gradient field $\partial\mathbf{v}/\partial\mathbf{x}$ inside the band can differ from the velocity gradient field $\partial\mathbf{v}^0/\partial\mathbf{x}$ outside:

$$\frac{\partial\mathbf{v}}{\partial\mathbf{x}} - \frac{\partial\mathbf{v}^0}{\partial\mathbf{x}} = \mathbf{g} \cdot \mathbf{n}. \quad (16)$$

In addition, continuing equilibrium requires that

$$\mathbf{n} \cdot \dot{\boldsymbol{\sigma}} - \mathbf{n} \cdot \dot{\boldsymbol{\sigma}}^0 = 0 \quad (17)$$

at incipient localization where $\dot{\boldsymbol{\sigma}}$ is the stress rate inside the band and $\dot{\boldsymbol{\sigma}}^0$ is that outside.

For the purpose of discussion, several simplification assumptions are made.

- (i) The stress state is uniaxial within constituent single crystals near the free surfaces.
- (ii) The multiple slip shear bands (i.e. macroscopic shear bands) initiate first within constituent crystals that are oriented for double or multiple slip.
- (iii) The classical bifurcation conditions listed in equations (16) and (17) are reasonable (i.e. the stress–strain gradient can be neglected).

Based on the above assumptions, the idealized double-slip model can be applied to understand the different localization conditions between the tensile and compressive side.

The idealized double-symmetric-slip model has been used extensively in studying the critical localization conditions (Asaro 1979, Bassani 1994, Dao and Asaro 1996a) in crystalline solids. There are two symmetric loading axes, that is vertical and horizontal, in the idealized model. As discussed by Asaro (1979), for fcc crystals, the angle between the slip plane and the symmetric loading axes may be assigned as $\phi_1 = 35^\circ$ and $\phi_2 = 55^\circ$ under uniaxial tension and compression respectively. If we denote θ as the shear band angle to be determined, following the procedures given by Asaro (1979) and Harren *et al.* (1988), assuming uniaxial loading conditions, the critical hardening conditions can be readily computed. Noting that the hardening decreases ($h > 0$ and $h \rightarrow 0$) as the strain increases, the first possible tensile shear band is expected at an angle $\theta = 40^\circ$ under tensile loading and $\theta = 50^\circ$ under compressive loading. Since the critical hardening rates predicted for the tensile and compressive sides are virtually the same, the macroscopic shear bands are expected to initiate at similar bending deformation levels. The predictions by this simple model, in terms of shear band angles and initiation conditions, are consistent with the experimental observations as well as the computational results. This is a double confirmation that the shear bands developed during bending are directly related to the crystallographic slip.

6.2. Concluding remarks

A combined experimental, computational and theoretical approach is taken to study the localization and fracture initiation modes in bending and hemming of sheet materials. A crystal-plasticity-based computational micromechanics model is constructed. To summarize the major findings obtained in this study, we conclude the following.

- (1) The computational and theoretical (bifurcation) results agree well with experimental observations:
 - (a) Crystallographic slip related intense shear bands and surface roughening are the natural outcome of the computational micromechanics model. Intense shear banding is found to be the major failure initiation mode by experimental observations.
 - (b) Localized deformation patterns predicted by the computational model agree well with the experimentally observed patterns. Intense shear bands initiate on or near the outer surface and from the lower points of surface roughness.
 - (c) Shear band angles (with respect to the free surfaces) are found to be around 40° on the tensile side and around 50° on the compressive side by the experimental observations, computational calculations and bifurcation analyses.
- (2) Certain new understanding is obtained from the numerical simulation work.
 - (a) Increased strain hardening reduces the intensity of strain localization, especially the intensity of sharp intense shear bands.
 - (b) Crystallographic rolling texture (with medium intensity) might increase surface roughening significantly.
 - (c) Constituent particles, especially those near the free surface, can significantly increase the localization intensity and the surface roughening.
 - (d) Two competing mechanisms are identified owing to the presence of hard particles, namely the *inhomogeneity* effect that increases the intensity of the non-uniform and localized deformation, and the *strengthening* effect that reinforces the neighbouring matrix material and limits the development of intense shear bands. The *inhomogeneity* effect is the dominant factor in most cases, especially at larger strain levels.

The understanding obtained using a systematic and quantitative approach may provide insight for alloy and process design to improve fracture resistance of aluminium alloys, in general, and bendability and hemmability of sheet alloys, in particular. For example, a random texture with higher hardening is preferred to delay the intense shear banding and failure initiation. Since the effects of the constituent particles below the free surface drop quickly versus the depth of these particles, the ‘cleanness’ near the surface of sheet material becomes more important.

In general, bendability and hemmability is primarily influenced by factors such as hardening (n value), constituent particles, grain-boundary precipitates and surface roughening. Bendability and hemmability can be enhanced by a higher n value, lower volume fraction, more uniformly distributed constituent particles, cleaner grain boundaries, smaller grain-boundary precipitates, smoother as-rolled surface and suppressed surface roughening in deformation.

Concerning the texture effects, it has been reported that surface roughening may be reduced with certain strong textures (Wilson *et al.* 1981). This is probably because the incompatibility between neighbouring grains is reduced. However, intense shear bands may initiate at lower strains for the strongly textured materials than for a random textured material (Becker 1998).

Future directions include the consideration of initial surface roughness, realistic textures (experimentally measured recrystallization and rolling textures), particle size and shape effects, particle fragmentation and debonding effects, and other materials and manufacturing parameters.

Like many problems found during the materials manufacturing processes, improvement in the fracture resistance of aluminium alloy, in general, and bendability and hemmability of sheet alloys, in particular, involves many factors that are not easily distinguishable through normal experimental methods. With the computational model, 'virtual experiments' can be performed, and the effects of individual parameters as well as the composite effects of these parameters can be studied and evaluated using a systematic and quantitative method. It is most beneficial to take an integrated approach that combines experimental, computational and theoretical studies.

ACKNOWLEDGEMENTS

The authors are grateful for the helpful and stimulating discussions with Daniel J. Lege, Larry A. Lalli, Frederic Barlat, Shawn J. Murtha and Hasso Weiland during the course of this study. Special thanks are due to Daniel J. Lege who critically read the draft of the manuscript.

REFERENCES

- ABAQUS, 1998, Theory Manual Version 5.8 (Pawtucket, Rhode Island: Hibbitt, Karlsson and Sorenson).
- ASARO, R. J., 1979, *Acta metall.*, **27**, 445.
- ASARO, R. J., and RICE, J. R., 1977, *J. Mech. Phys. Solids*, **25**, 309.
- ASHBY, M. F., and VERRALL, R. A., 1977, *Phil. Trans. R. Soc. A.*, **228**, 59.
- BASSANI, J. L., 1994, *Adv. appl. Mech.*, **30**, 191.
- BEAUDOIN, A. J., BRYANT, J. D., and KORZEKWA, D. A., 1998, *Metall. Trans. A.*, **29**, 2323.
- BECKER, R., 1992, *J. appl. Mech.*, **59**, 491; 1998, *Acta mater.*, **46**, 1385.
- BECKER, R., and PANCHANADEESWARAN, S., 1995, *Acta metall.*, **43**, 2701.
- CHANG, Y. W., 1979, PhD Dissertation, Brown University, Providence, Rhode Island.
- CHANG, Y. W., and ASARO, R. J., 1981, *Acta metall.*, **29**, 241.
- CUITINO, A. M., and ORTIZ, M., 1993, *Modeling Simulation Mater. Sci. Engng.*, **1**, 225.
- DAO, M., and ASARO, R. J., 1996a, *Mech. Mater.*, **23**, 71; 1996b, *ibid.*, **23**, 103.
- DAO, M., LEE, B. J., and ASARO, R. J., 1996, *Metall. Trans. A.*, **27**, 1996.
- DEVE, H. E., HARREN, S. V., MCCULLOUGH, C., and ASARO, R. J., 1988, *Acta metall.*, **36**, 341.
- GRAF, M., and HORNBOGEN, E., 1977, *Acta metall.*, **25**, 883.
- HADAMARD, J., 1903, *Lecons sur la Propagation des Ondes et les Equations de L'Hydrodynamique* (Paris: A. Hermann), Chapter 6.
- HARREN, S. V., DEVE, H. E., and ASARO, R. J., 1988, *Acta metall.*, **36**, 2435.
- HILL, R., 1962, *J. Mech. Phys. Solids*, **10**, 1.
- KALIDINDI, S. R., BRONKHORST, C. A., and ANAND, L., 1992, *J. Mech. Phys. Solids*, **40**, 537.
- LI, M., 2000 (in preparation).
- LI, M., and BUTLER, J. F., JR, 1999, *The Integration of Material, Process and Product Design*, edited by N. Zabarás *et al.* (Rotterdam: A. A. Balkema), p. 47.
- LI, M., and LEGE, D. J., 1997, Report ATC 97-481-06, Alcoa.
- McHUGH, P. E., ASARO, R. J., and NEEDLEMAN, A., 1993, *Acta metall.*, **41**, 1461.

- PEIRCE, D., ASARO, R. J., and NEEDLEMAN, A., 1983, *Acta metall.*, **31**, 1951.
- RAJ, R., and ASHBY, M. F., 1975, *Acta metall.*, **23**, 653.
- RICE, J. R., 1977, *Proceedings of the 14th IUTAM Conference on Theoretical and Applied Mechanics*, edited by W. T. Koiter (Amsterdam: North-Holland), p. 207.
- TRIANAFYLLIDIS, N., and NEEDLEMAN, A., 1982, *Int. J. Solids Struct.*, **2**, 121.
- TVERGAARD, V., 1987, *Mech. Mater.*, **6**, 53.
- VALKONEN, A. E., 1987, PhD Dissertation, Department of Metallurgical Engineering, Ohio State University, Columbus, Ohio.
- WILSON, D. V., ROBERTS, W. T., and RODRIGUES, P. M. B., 1981, *Metall. Trans. A.*, **12**, 1595.
- WU, T.-Y., BASSANI, J. L., and LAIRD, C., 1991, *Proc. R. Soc. A*, **435**, 1.